AIP Journal of Applied Physics

Characterization of a hollow core fibre-coupled near field terahertz probe

M. Misra, Y. Pan, C. R. Williams, S. A. Maier, and S. R. Andrews

Citation: Journal of Applied Physics **113**, 193104 (2013); doi: 10.1063/1.4804952
View online: http://dx.doi.org/10.1063/1.4804952
View Table of Contents: http://scitation.aip.org/content/aip/journal/jap/113/19?ver=pdfcov
Published by the AIP Publishing

Characterization of a hollow core fibre-coupled near field terahertz probe

M. Misra,[1,a)] Y. Pan,[1] C. R. Williams,[1] S. A. Maier,[2] and S. R. Andrews[1,b)]
[1]*Department of Physics, University of Bath, Bath BA2 &AY, United Kingdom*
[2]*Department of Physics, Imperial College London, London SW7 2AZ, United Kingdom*

(Received 26 February 2013; accepted 29 April 2013; published online 20 May 2013)

We describe the design and performance of a freely positionable THz near field probe based on a hollow core photonic crystal fibre-coupled photoconducting dipole antenna with an integrated sub-wavelength aperture. Experimental studies of the spatial resolution are compared with detailed finite element electromagnetic simulations and imaging artefacts that are a particular feature of this type of device are discussed. We illustrate the potential applications with descriptions of time domain near field studies of surface waves on a metamaterial and multimode propagation in a parallel plate waveguide. © *2013 AIP Publishing LLC*. [http://dx.doi.org/10.1063/1.4804952]

I. INTRODUCTION

Technology and applications in the terahertz frequency band (0.1–10 THz) have advanced considerably in the last two decades, largely as a result of the development of highly sensitive time domain spectroscopy and measurement techniques in the late 1980s and early 1990s which provided dramatically enhanced capabilities.[1] In THz time domain measurements, short pulses of radiation are typically generated by the optical excitation of transient photocurrents in semiconductors or displacement currents in nonlinear optical materials. The electric field of this broadband radiation is coherently detected using time delayed optical sampling in photoconducting antennas or electro-optic crystals such that amplitude and phase information are obtained as a function of time. Not long after the development of these powerful techniques, THz time domain imaging using simple focusing optics and raster scanning of the test object was demonstrated by Hu and Nuss.[2] Imaging at terahertz frequencies is now being explored for real world applications in pharmaceutical, semiconductor, and polymer quality control and has potential longer term uses in medical diagnosis and security screening.[1] There are also a large number of scientific uses because many materials have characteristic dielectric properties associated with vibrational modes or electronic band gaps at THz frequencies and THz radiation is also an excellent probe of the high frequency conductivity.[1]

The diffraction limited resolution of conventional far field THz imaging is a significant fraction of one mm at 1 THz, which is a considerable limitation in many applications. Development of near field probing and microscopy techniques are necessary to obtain higher spatial resolution. This is more challenging than at optical or microwave frequencies because of the combination of generally lower source power and less sensitive detection. Apart from a few material studies, time domain near field THz techniques have principally been employed to characterize simple metal-dielectric structures such as sub wavelength apertures,[3] metamaterials[4] and waveguides.[5] Particularly, useful information can be obtained from near field studies of THz waveguides where the mode structure can be revealed more directly than in far field measurements. An accurate knowledge of the near field is also crucial for the emerging area of designer THz surface guiding based on the spoof surface plasmon polariton concept.[6,7] Spatial resolution of order a few tens of microns is usually sufficient for device characterization, whereas sub-micron resolution is desirable for the study of materials.

The THz near field techniques studied so far can be broadly divided into two classes: those using apertures and those which are "apertureless." In the former, a sub-wavelength dimension physical aperture such as a hole in a metal sheet,[8] the exit of a tapered metal waveguide[9,10] or an optically excited region of high attenuation in a semiconductor film[11] is placed in front of a larger source or detector. It is also possible to use an intrinsically sub-wavelength dimension source or detector such as a microfabricated photoconducting antenna.[12,13] Another technique is to tightly focus femtosecond laser pulses into a thin nonlinear optical crystal to generate THz radiation in the focal volume by difference frequency generation[14] or detect it by reflective electro-optic sampling (EOS).[3] Nonlinear optical and electro-optical approaches have some advantages compared with photoconducting dipole antennas. For example, the crystallographic orientation provides a choice of the generated or detected THz polarisation and the fundamental source or detector size is comparable to the laser focal spot size which could be of the order of a few microns. The only necessary fabrication step is the deposition of a high reflectivity coating for the optical beam. This technique is also less prone to imaging artefacts, as discussed further below, although its greater sensitivity to laser noise makes achieving high dynamic range challenging.[15] The spatial resolution of both the all-optical and antenna based techniques is limited by a combination of source or detector geometry and sample-probe separation and is typically of order 5–20 μm near 1 THz. In the apertureless approach, THz radiation is scattered at the end of a sharp metal probe tip and detected in the far field.[16,17] Significantly higher resolution, ultimately comparable with the radius of curvature of the tip, can in principle be achieved by this method,[18] although generally with large,

[a)]Present address: SRM University, Lucknow, India.
[b)]Electronic mail: s.r.andrews@bath.ac.uk

problematic background signals and a low signal to noise ratio.

In this paper, we describe the design and performance of a THz near field probe, comprising a photoconducting antenna with integrated aperture, which we have developed to perform time domain microscopy with a few tens of μm resolution to assist in the characterisation of pulsed terahertz sources and waveguides. Fibre delivery of optical probe pulses to the THz receiver allows free positioning during imaging without change in the pulse timing. Combined with the use of a fibre coupled transmitter, changes in experimental geometry are very straightforward. We describe the characteristics and advantages of hollow core photonic crystal fibre for this application and discuss the spatial resolution of the system. We illustrate the system's potential applications with studies of two different THz waveguides. The first involves surface waves on a metamaterial comprising an array of blind cylindrical grooves in a metal sheet and the second examines waveguiding between parallel metal plates with a step discontinuity in plate separation. Here, the guide and THz source are fixed in position, whilst the detector is scanned over the output face. A major problem in any kind of near field microscopy lies in understanding the effect of the probe on the system under study. The sample-probe interaction in the electro-optic sampling case has been briefly considered by Guestin *et al.*[19] In general, field reconstruction requires prior knowledge of both sources and scattering objects. Another purpose of this paper is to examine such effects in the case of planar photoconductive probes. We have reported a short account of this aspect previously.[20]

II. EXPERIMENTAL DETAILS

A. The photoconductive probe

The near field probes that we have studied are based on low temperature grown GaAs photoconducting dipole detectors illuminated through integrated sub-wavelength apertures and are similar to ones previously described by Mitrofanov and co-workers[8] except for the absence of a GaAs tip protruding through the aperture and a smaller separation between aperture and antenna. The photoconducting material consists of a 1.5 μm thick low temperature GaAs epilayer grown on a 650 μm thick semi-insulating GaAs substrate with an intervening 100 nm AlAs etch stop layer. Carrier lifetimes and THz mobility, measured by optical pump-THz probe time domain spectroscopy on epilayers transferred to sapphire substrates are in the range 300–400 fs and 2500–3500 cm^2/Vs, respectively. The probes were fabricated as follows. A pair of dipole antennas, typically of length 10 μm with 5 μm wide photoconducting gaps and 10 μm wide connecting leads was first deposited on 6 mm $\times$ 6 mm chips taken from the LT GaAs wafer. The two dipoles are separated by 200 μm and are experimentally determined to be electrically and optically independent. Chips were then glued, metal side down, to 1 mm thick, 6 mm diameter, optically polished, polycrystalline sapphire substrates using a few μm thick layer of low viscosity epoxy[21] which is UV cured whilst the chip and substrate are in hard contact in a mask aligner. The wafer back side was then thinned down to the AlAs layer using wet etching to remove the first 600 μm of GaAs, followed by selective reactive ion etching using a mixture of SF_6 and $SiCl_4$. Etching terminated at the AlAs layer, leaving a mirror-like surface. The AlAs was then removed in dilute HF and connection pads to the dipole antennas were exposed by further patterning and wet etching of the LT GaAs layer. To complete the device, a 500 nm thick SiO_2 insulating layer and a 300 nm thick, 2 mm square aluminium screen with apertures were finally deposited by electron beam evaporation. The apertures were 10, 20, 50, or 100 μm square and centred over the dipoles to an accuracy of ± 2 μm The aluminium screen is more than four times thicker than the penetration depth at 1 THz so that any background signal is reduced by a sufficient factor of more than one hundred. It should be noted that the epoxy layer has poor thermal conductivity. Care needs to be taken to ensure that it is as thin as possible in order to avoid blistering caused by local heating of the photoconducting layer when exposed to the receiver gating beam. By trial and error, we found that a safe upper limit on gating power for our probes was 8 mW when focused to a 5 μm spot. At this power, the noise for a 10 μm dipole was $\sim$280 fA/$\sqrt{}$Hz at a signal modulation frequency of 2 kHz, consistent with the average "on" resistance of 2.5 MΩ and a dominant thermal noise mechanism. A factor of two or more improvement in signal to noise ratio could be achieved by changing the design to allow higher gating powers. Such powers could be tolerated if the epoxy attaching the photoconductor to the substrate was eliminated. For example, an epitaxial lift-off and van der Waal's bonding technique could be used to attach the LT GaAs epilayer directly to the sapphire.[22]

The devices were electrically contacted by polishing two bevels on the sapphire substrate and laying down metal tracks to take the connection pads below the plane of the dipoles. Finished devices were waxed onto the end of interchangeable, hollow 10 mm diameter machinable glass cylinders, each containing a 6 mm focal length, 0.3 numerical aperture (NA) aspheric focusing lens. The probe assembly can be freely rotated about its cylindrical axis to align the dipole arms with the field being studied. A 0.3 NA aspheric collimating lens feeds light from the fibre end facet to the focusing lens with an intermediate beam splitter, photodiode and miniature camera to allow optimisation of fibre coupling and alignment of the gating beam to the antenna. The fibre is held by a miniature 1 μm resolution triple axis manipulator to allow focusing and alignment of the gating beam with the photoconducting antennas. The complete assembly, which is about 75 mm long, is mounted on a motorised, 3-axis stage, as shown schematically in Fig. 1(a).

B. Optical fibre pulse delivery

Optical pulses from a Ti:sapphire oscillator were delivered to the probe and transmitter using hollow core photonic crystal fibre (PCF).[23] The PCF was made for photonic bandgap guiding near 800 nm and has been described previously.[24] The fibre (Fig. 2(b) inset) has an 8 μm diameter core surrounded by 8 rings of holes and a numerical aperture (NA) of 0.15. Similar fibres are available commercially.

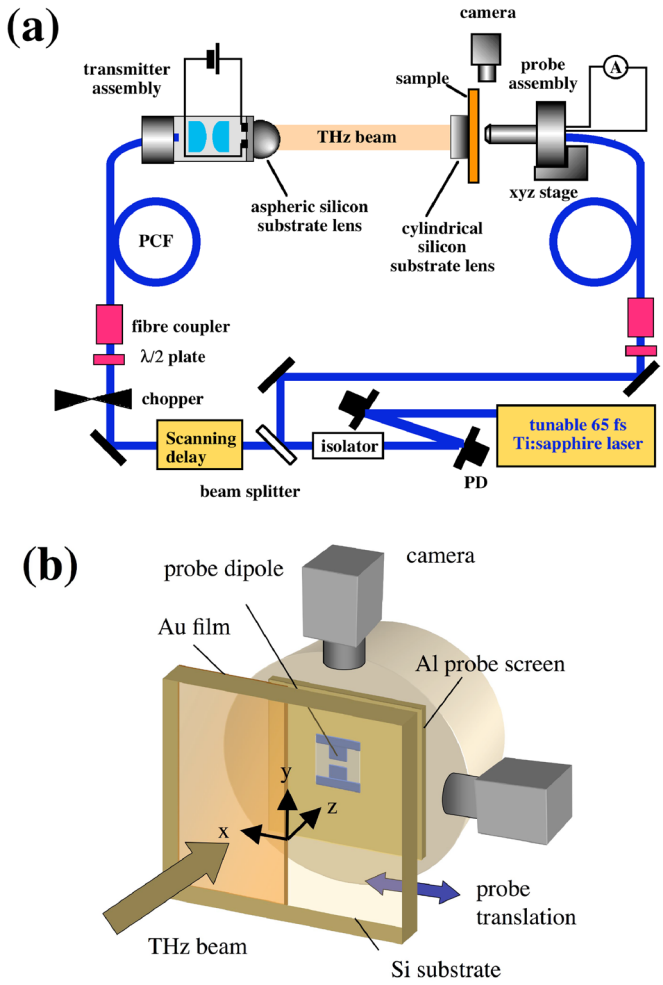

FIG. 1. (a) Schematic of experimental arrangement for testing spatial resolution. PD denotes quadrant photodiode. (b) Detail of test sample and tip of probe (Si substrate shown transparent) showing coordinate system referred to in the text.

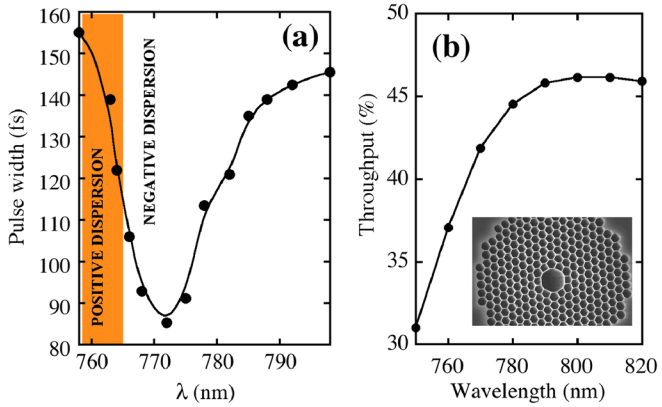

FIG. 2. (a) Pulse width at output of 1.5 m length of HCPF measured by interferometric autocorrelation and assuming a sech^2 envelope. The zero dispersion wavelength is 765 nm and the input pulse bandwidth is 10 nm. (b) Typical throughput of a 1.2 m long fibre. The inset shows an electron micrograph of a cleaved fibre end.

Although the fibre is not intrinsically single mode, fundamental mode propagation is achieved with optimum coupling and the 1.2 m fibre lengths used in our system. The advantages of this type of fibre compared with the solid core ones conventionally used[25–27] are threefold.

First, the laser centre wavelength can be chosen so that the second order fibre dispersion is very small or negative, thus eliminating the requirement for dispersion compensation using a pair of gratings which is essential when using solid core fibre. The PCF has zero second order dispersion near the band edge and negative waveguide dispersion at longer wavelengths, within the high transmission band. The laser centre wavelength can thus be chosen so that the combined positive dispersion of bulk optical components in the system, such as optical isolators, beam splitters and lenses, is exactly balanced by negative dispersion in the fibre. The minimum pulse duration and thus maximum potential terahertz bandwidth are therefore achieved at a centre laser wavelength just above the short wavelength band edge of the fibre, as shown in Fig. 2(a). The minimum pulse duration of 85 fs is larger than the bandwidth limit of 65 fs, probably because of the proximity to the band edge relative to the pulse bandwidth, and third order fibre dispersion. The maximum fibre transmission is found at a higher wavelength of around 800 nm (Fig. 2(b)) so that the system was typically operated at 778 nm with a bandwidth of 5 nm in order to optimise the signal strength. Second, because guiding is largely in the air core, self phase modulation in the fibre can be neglected for pulse energies at the few nJ level. This means that power fed to the transmitter and receiver can be optimised for the devices rather than being constrained by the fibre. We used 1 nJ for exciting the transmitter and 0.1 nJ for the receiver. In conventional single mode fibre, the energy of 100 fs pulses must typically be kept below 0.1 nJ to avoid significant temporal broadening due to self phase modulation.[25] Hollow core fibre of the current design can be used with 100 fs pulse energies up to at least a few hundred nJ.[24] Their compatibility with high optical pulse energies could be particularly advantageous when using larger area, inter-digitated array transmitters,[28] which can exploit the extra energy available from extended cavity oscillators or high repetition rate regenerative amplifiers. Third, reflection of light from the air core is very weak so that an optical isolator, normally used to prevent reflection back into the laser and interruption of mode locking, is not strictly needed although it can be useful during initial alignment.

We should mention some minor disadvantages of PCF, namely coupling and propagation losses and sensitivity to atmospheric water vapour. Using a conventional telescope arrangement and a 10× magnification, 0.2 NA microscope objective to match the pump and probe laser beams to the fibre NA and core size, the throughput of 1.2 m lengths of good fibre was typically in the range 40%–50%, as shown in Fig. 2(b). Transmission was limited by imperfect spatial matching of the free space and guided modes and an intrinsic attenuation of ~1.5 dB/m. Unintentional fabrication defects, such as dust incorporation at the pre-form fabrication stage, can result in worse performance. Good lengths of fibre can be selected by looking for the absence of bright spots with an infra-red viewer under optimum guiding conditions. A more serious problem is that the fibre transmission slowly degrades in the presence of atmospheric water vapour, which tends to penetrate the cores. This is avoided in our system by

enclosing the fibres in the same dry air purged and dust filtered enclosure as the THz beam path. The same lengths of fibre have been in use for more than a year without degradation. An alternative method of reducing the ingress of dust or moisture is to splice the PCF to a short lengths of conventional single mode fibre.[29] This technique would also allow the fibres to be glued directly to the transmitter and receiver chips which would allow further miniaturisation and improve stability.

Half wave plates placed before the fibre couplers in Fig. 1(a) allow the optimum input polarization for the fibre which is usually slightly birefringent because of unintentional ellipticity in the core profile. The output ends of the fibres are rotated to so that the polarization is perpendicular to the metal tracks of the transmitter and receiver, a geometry which optimises their efficiency.[30] The transmitter consists of a conventional biased stripline fabricated on LT GaAs with a 50 μm track separation and a 12 mm diameter collimating silicon substrate lens. The positive track edge is illuminated using a 50 μm $\times$ 3 μm line focus.[31] The lens is aspheric for maximum collection efficiency.[32] Fig. 1(a) shows a schematic of the system. The optical system is very stable with respect to handling of the fibres and in daily use requires little more than small changes to the alignment of the beam from the femtosecond oscillator which is achieved with the help of signals from quadrant photodiodes on the backs of two dielectric mirrors whose centres define the input optical axis.

III. ELECTROMAGNETIC MODELLING

Three dimensional time domain electromagnetic simulations were performed on various sample-probe systems and compared with experiment to better understand the properties of the probe. These simulations used the finite integration technique.[33] For example, in the calculations of the probe's spatial resolution, the interaction of a 3 THz bandwidth plane wave with the probe positioned in close proximity to a test structures was modelled on a variable mesh size with 80 $\times$ 10^6 cells over a 1 $\times$ 1 $\times$ 0.5 mm^3 simulation volume including every sample and device layer. The dielectric function of the illuminated low temperature GaAs photoconducting gap was treated in the Drude model with a plasma angular frequency of 2.4 $\times$ 10^{14} rad/s and a scattering time of 55 fs. The carrier density is inferred from the experimental optical gating power of 8 mW and determined the scattering time is deduced from the THz mobility of 3000 cm^2/Vs. The conductivity of the photoconductor was assumed constant for the duration of the terahertz transient. Although this does not correctly account for the frequency dependence of the real probe, which samples the signal in a finite time window of order the photocarrier trapping time of ~350 fs, it does not significantly affect calculations of the spatial variation of the probe signal. The dipole antenna arms were treated in a Drude model for gold with a plasma frequency of 1.4 $\times$ 10^{16} rad/s and a scattering time of 25 fs.[34] The silicon dioxide, epoxy and semi-insulating GaAs layers were assumed to be loss free and the remaining metal layers were generally modelled as perfect electric conductors (PECs). Modelling the metal parts of the aperture screen or sample as real conductors in a Drude model or allowing for field penetration analytically using Leontovich surface impedance matching boundary conditions[35] gave results that were not significantly different to the PEC case. Surface plasmon effects are very small, which is not expected considering that the penetration into the metal is less than 100 nm, whilst the wavelength in air is of order a hundred microns or more. The simplified assumption of perfectly conducting metals hugely speeds up the electromagnetic simulations.

IV. PROBE PROPERTIES

A. Sensitivity and frequency response

Fig. 3(a) compares time domain signals of probes fabricated with and without apertures under broad area illumination. The receiver current is proportional to the component of the electric field in the middle of the probe aperture that is parallel to the dipole arms to a good approximation. The most

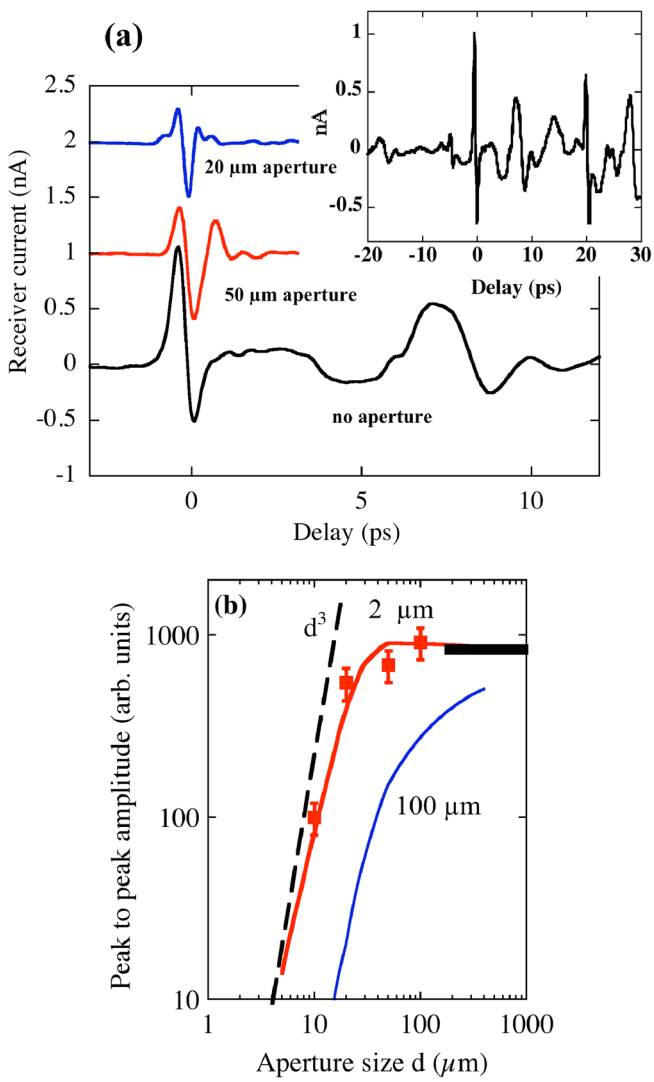

FIG. 3. (a) Examples of measured signals for the same source and geometry but different aperture sizes. The inset shows the case with no aperture on an extended time scale. (b) Measured (squares) variation of peak to peak signal amplitude with aperture size. The solid curves show the calculated variation for the antenna placed $s = 2\,\mu$m (as in experiment) and, for comparison, $s = 100\,\mu$m behind the aperture. The dashed line shows the expected trend in the far field. The horizontal bar shows the signal amplitude with no aperture.

noticeable features are the small reduction in signal strength for an aperture size of 20 μm compared with the apertureless case and the different shape of the signals with apertures, which are similar to the time derivative of the apertureless signal. The first point is considered again in Fig. 3(b) which shows the variation of peak to peak signal amplitude evaluated experimentally and numerically for an antenna-aperture spacing of $s = 2\,\mu$m. Because the wavelength is much larger than the aperture size d, the dipoles are located in the very near field zone of the aperture, $s < d/2$.[36] This gives good sensitivity since in this region the field behind the aperture is predominantly evanescent and decrease slowly with decreasing d.[36,37] For example, reducing d from 50 to 20 μm results in only a factor of two measured reduction in signal strength near 1 THz. For very small apertures or large values of s, Fig. 3(b) shows that the variation of field with aperture size tends to the d^3 dependence expected in the far field.[36,37]

The second point is explored further in Fig. 4(a) which shows the change in spectrum with aperture size for the same source. To a first approximation, the aperture acts as a high pass filter with a cut off frequency that simply increases with decreasing aperture size, as observed previously.[3,38] In the time domain, a high pass filter is equivalent to a signal differentiator, thus explaining the relative shapes of the traces obtained with and without apertures in Fig. 3(a). The calculated relative transmission, which includes the effects of the dielectric and antenna filling the aperture, is shown in Fig. 4(b). Relative aperture transmission in Fig. 4(b) is defined as the ratio of the electric field at the centre of the photoconducting gap with the aperture in place to that with no aperture. The response of the integrated antenna and aperture is more complicated than that of a simple cut off filter, with a useful enhancement of the transmission near the cut off frequency clearly evident.

B. Spatial resolution and imaging artefacts

For antennas with apertures smaller than or comparable with the dipole length, the spatial resolution fundamentally depends only on the aperture size and is independent of frequency.[39] Perhaps the simplest way to experimentally quantify the resolution is to perform a one dimensional, constant

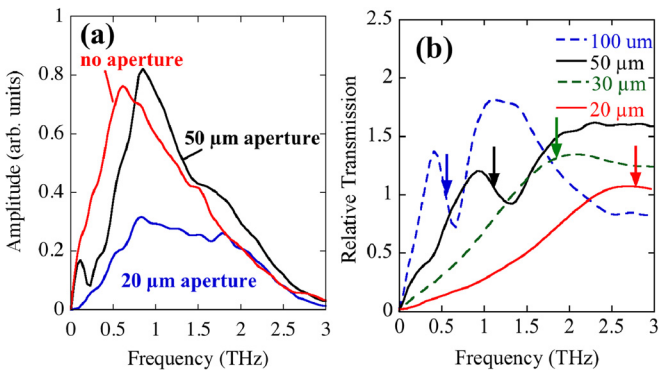

FIG. 4. (a) Examples of experimental spectra for the same source and geometry but different aperture sizes, using a common amplitude scale. (b) Calculated frequency dependence of aperture transmission relative to the response with no aperture for aperture sizes shown. The vertical arrows indicate the cut of frequencies for infinitely long square waveguides with the same lateral dimensions as the apertures.

height scan of the probe across and in very close proximity to a "knife edge" placed in a THz beam. We manufactured such a "knife edge" by depositing a large area (6 mm × 6 mm), 200 nm thick, Ti/Au film on the front side of a 500 μm thick, high resistivity silicon wafer. The substrate was illuminated from the back using a hyper hemicylindrical silicon lens (Fig. 1(a)) such that the long axis of the 8 mm × 300 μm focused beam was aligned with the probe scanning direction. The peak amplitude of the incident THz field is constant to within ±5% over the central 2 mm of the beam along the scan axis. The sample's metal film thickness is sufficient to attenuate the incident THz field by a factor of order 100.

The probe was initially placed a few hundred μm in front of the sample and its plane visually aligned parallel to that of the test object using two orthogonal cameras with a 3 cm working distance. At such separations, a reflection was clearly distinguished as an echo in the time domain signal. A series of time domain traces at varying sample-probe separation was then be used to calibrate the probe-substrate separation to a typical precision of ±1 μm. The orientation of the test substrate was subsequently refined so that the delays of the reflected signal at three corners of the desired scan area were identical, thus ensuring parallelism between the probe and sample planes. This technique allows the probe to be safely and precisely brought to within 10 or 20 μm of the test object surface and scanned over distances of several mm. It is important to note that this method is restricted to planar samples with large unmetallized areas so that accurate control and knowledge of the probe-sample parallelism and separation in the general case is a challenge. Indeed, it is currently much more of a problem when using planar probes than is poor signal strength. In some cases, this can be avoided by bringing the probe into sliding contact with the object but there is then the risk of damage to the sample or to the fragile probe. These problems are much less severe with apertureless, needle geometry probes which are easily replaced and can in principle utilise sophisticated approach techniques borrowed from shear force and other scanning probe microscopies.[40]

Figures 5(a) and 5(b) show experimental line scans across the metal edge of the test sample at fixed delay for sample-probe separations of 20 μm and 50 μm and incident polarizations along y (parallel to the edge) and along x (perpendicular to the edge). For each polarization, the dipole antenna is oriented for maximum signal. The sharpness of the cut off as the probe travels behind the metal of the test sample clearly depends not only on the distance between the planes containing the edge and the probe aperture but also on the polarization of the THz beam. This effect was originally noted by Hunsche *et al.*[9] and Mitrofanov *et al.*[8] but not explained at the time. For polarization parallel to the metal edge, the distance between the 10% and 90% amplitude points is approximately equal to the sum of aperture size and sample-probe gap. For the perpendicular polarisation, the apparent resolution is significantly worse and the signal additionally exhibits increasing delay with increasing positive x. Figs. 5(c) and 5(d) confirm that the spatial resolution is independent of frequency in both polarizations.

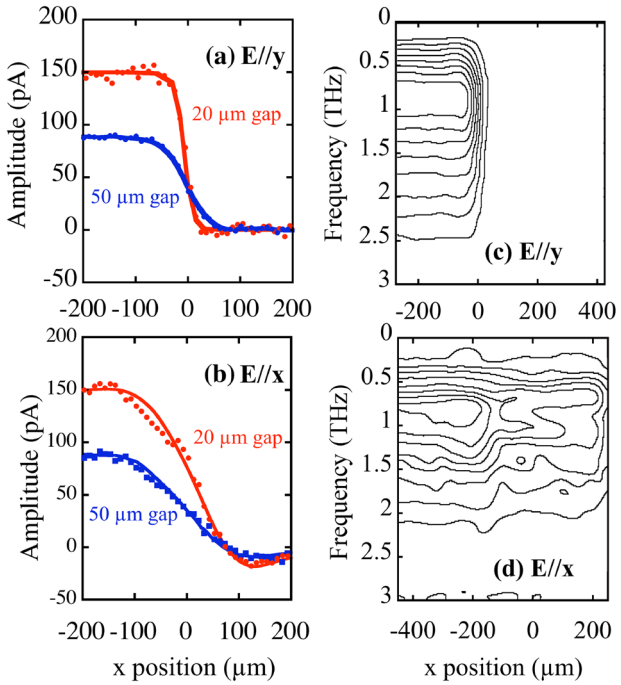

FIG. 5. Measured (points) and calculated (solid curve) peak electric field amplitude at a fixed delay corresponding to the peak THz signal at large negative x for incident THz polarisation (a) parallel and (b) perpendicular to test metal edge over which a 10 μm probe with 20 μm aperture is scanned at a constant gap of 20 μm or 50 μm. (c), (d) Evenly spaced, constant Fourier amplitude contours obtained from signal spectra at a gap of 20 μm. Parts (a) and (b) reprinted with permission from Appl. Phys. Lett. **100**, 191109 (2012). Copyright 2012 American Institute of Physics.

The reason for the different behaviour for incident $E//x$ and $E//y$ can be understood with the aid of the field maps in Figs. 6(a) and 6(b) which show the calculated time average of E_x and E_z, respectively, for incident polarization perpendicular to the gold edge ($E//x$). It is apparent that E_x falls off quickly in the shadow of the gold film, in a very similar manner to that for $E//y$ (Fig. 5(a)), but grows again in the region of the aperture. It is also apparent that diffraction at the gold edge very efficiently couples the x-polarised incident wave into the z polarized TEM (TM_0) mode of the parallel plate waveguide formed between the metallic sample and probe surfaces. Such coupling does not occur for the orthogonal incident polarization. In the experiment, the TEM mode propagates over relatively large distances with only a small change in amplitude due to Ohmic loss and lateral spread of the guide wave associated with the finite width of the incident THz beam. The guided mode has no cut-off and negligible z variation of electric field within the waveguide. For sample-probe separations of 50 μm or less, higher order TM modes are cut off within the 3 THz system bandwidth. The importance of this waveguiding effect lies in the fact that the dipole and aperture together diffract part of the TEM mode to generate an additional contribution to E_x at the antenna proportional to the instantaneous difference in E_z across the aperture.[41] The measured signal is thus proportional to $E_x(t) + adE_z(t)/dx$, where a is a constant proportional to the aperture size. The calculated current in the dipole arms accurately reproduces the shape of the fixed delay curves, as shown in Figs. 5(a) and 5(b). The vertical axis in the calculations is adjusted to match experiment using a single scaling factor. Generally, there is no similar cross polarization effect when using EOS. This makes image analysis much easier and is a significant advantage.

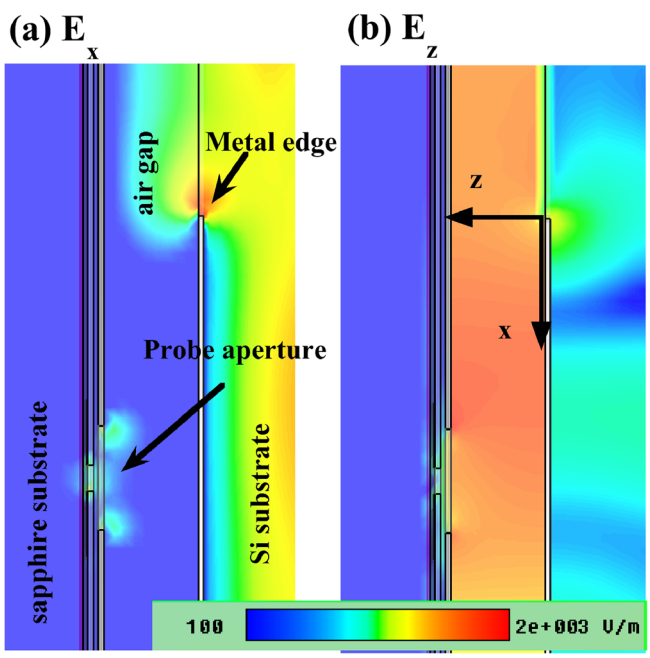

FIG. 6. Time average E_x (a) and E_z (b) field maps near the probe aperture and test metal edge for incident polarisation parallel to x and a 20 μm sample-probe separation.

A further check on the ability of the calculations to describe experiment is obtained by comparing measured and predicted results for the peak to peak field versus x. Fig. 7(a) shows that there is again good agreement with only a single amplitude scaling factor. The initial fall off in peak to peak signal for $E//x$ as the probe moves further into the shadow of the gold film is explained by the evolution of $dE_z(t)/dx$ as the wave in the gap between probe and sample evolves from the incident plane wave into the TEM-like guided mode. The x-derivative of $E_z(t)$ for the TEM mode is constant in the absence of attenuation or lateral wave spreading. There is,

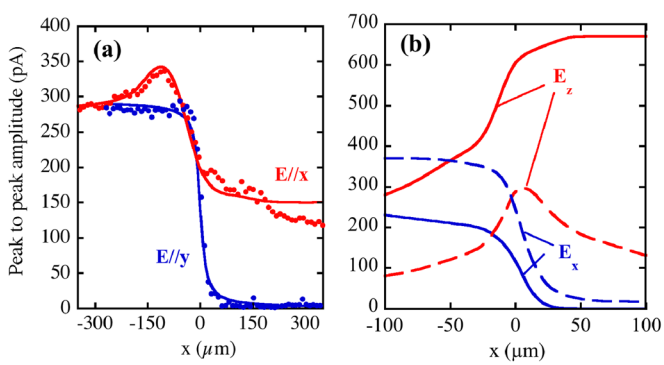

FIG. 7. (a) Measured (points) and calculated (solid curve) peak to peak amplitude of the receiver current for THz polarisation parallel (E//y) and perpendicular (E//x) to test metal edge over which a 10 μm probe with 20 μm aperture is scanned at a constant height of 20 μm. (b) Calculated fields 10 μm in front of the sample with (solid curves) and without (dashed curves) the probe which is treated as a uniform metal sheet. Reprinted with permission from Appl. Phys. Lett. **100**, 191109 (2012). Copyright 2012 American Institute of Physics.

therefore, a discrepancy between experiment and prediction for positive x in that the measured signal does not tend to a constant value. This is because in the simulation the incident THz beam is a plane wave so that lateral spreading due to the line focus illumination used in the experiment is not taken into account. We note that treating the metal conductivity in a more exact Drude model in which surface plasmon polaritons (SPPs) are supported yields results which are not noticeably different to the PEC case in which there is no field penetration into the metal and thus no SPPs.

In order to fully understand the perturbing effect of the probe on the field in front of the test sample, it is illuminating to compare the field distributions with and without the probe. For computational simplicity, we use the PEC approximation and substitute the probe by a uniform metal sheet with a sample-probe separation of 20 μm. Fig. 7(b) shows the field 10 μm in front of the sample for incident polarization along x. The main perturbing effects of the probe are a spatially uniform screening of E_x and the generation of a much larger z field component with a different spatial variation to that in the probeless case.

C. Apertureless photoconducting probes

There have been several reports of near field studies using planar photoconducting dipoles without apertures.[4,12,42,43] Such antennas are easier to fabricate than ones with integrated apertures and the dynamic range is somewhat larger so that it is important to compare their spatial resolution. We therefore performed similar resolution tests to those described in Sec. IV B on an apertureless probe with a 10 μm dipole of the same pattern described earlier. Results for the peak to peak signal are shown in Fig. 8(a). Again, there are marked differences between the results for incident polarization parallel and perpendicular to the metal edge of the test sample which are accurately reproduced by the calculations. Energy is still coupled, albeit less efficiently, into a z-polarised propagating wave in the space between the probe and sample, as shown in Fig. 8(b). This wave can generate a significant in-plane field across the dipole by scattering at the antenna alone. Fig. 8(b) also shows that the x component of the field varies more slowly with x than it does for the probe with aperture.

We now compare the spatial resolution of probes with and without apertures in detail for the most favourable polarization. For an apertureless 10 μm dipole probe, experiment (Fig. 8(c)) and simulation shows that the spatial resolution at 20 μm sample-probe separation is similar to that for the same probe with a 20 μm aperture at a larger separation of 50 μm. This suggests that the resolution is about 30 μm worse. Previous studies using a similar apertureless dipole have suggested a higher spatial resolution than this[43] and we conjecture that the resolution might in some cases be enhanced by coupling between the sample and probe if the latter has electromagnetic resonances within the probe bandwidth. Also of note is the large low frequency "background" and additional fast structure evident in the signal from the apertureless probe shown in Fig. 3(a) which we believe comes from a combination of radiation by-passing the transmitter lens, reflections off the rear of the sapphire probe substrate and coupling to leaky modes of the coplanar stripline that provides connections to the arms of the dipole. Probes with integrated apertures can thus offer higher spatial resolution and cleaner signals with only a small reduction in sensitivity. In Sec. V, we describe two experimental investigations of waveguiding using this type of probe.

V. EXAMPLE INVESTIGATIONS

A. Near field probing of surface waves on a structured metal surface

To explore the frequency resolved imaging capabilities of the probe, we studied guided wave propagation on a metamaterial surface. Metamaterials are metal-dielectric composite materials with electromagnetic properties that can be tailored by engineering the geometrical structure on subwavelength scales. At THz frequencies, they are being explored for applications such as sensors, filters, and waveguides. Here, we have designed and fabricated a microstructured surface to guide surface waves which mimick

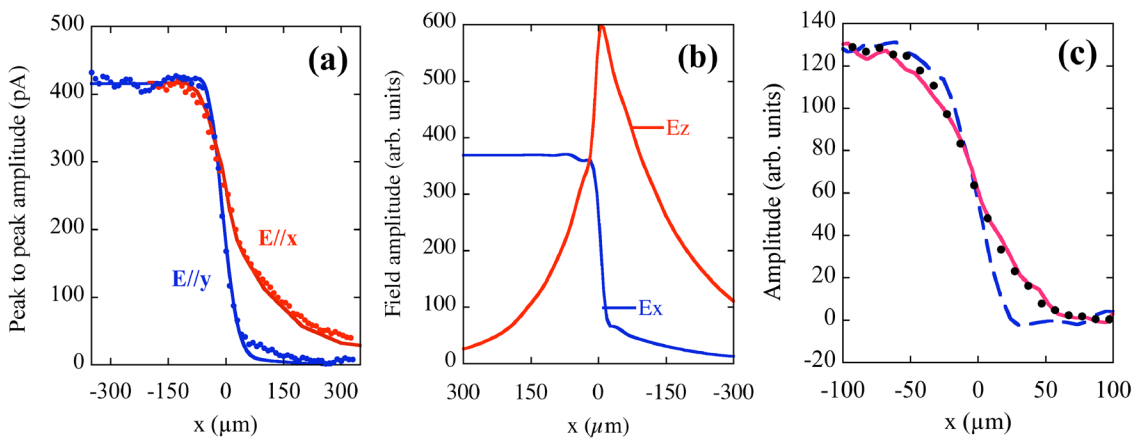

FIG. 8. (a) and (b) show peak to peak signals versus probe position for a 10 μm apertureless probe and 20 μm probe-sample separation. In (a), experimental (points) and calculated (curves) signal amplitudes are shown for polarisations perpendicular (E//x) and parallel (E//y) to metal test edge. In (b), the calculated variation of fields in the middle of the gap is shown. (c) Measured peak signal amplitude at fixed delay for THz polarisation parallel to metal edge (E//y) at a probe-sample separation of 20 μm for the apertureless probe (points) and the probe with 20 μm aperture (dashed curve). The solid curve shows results for the 20 μm probe at a larger probe-sample separation of 50 μm.

SPPs.[6] The guided modes are tightly bound to the surface and propagate in two bands. Electron micrographs of the structure, whose far field properties have been described previously,[44] are shown in Figs. 9(a) and 9(b). It consists of a 60 μm thick sheet of patterned and cured epoxy based SU-8 photoresist,[45] conformally coated with copper and supported on a 500 μm thick Pyrex substrate. The high aspect ratio pattern consists of a square $\Lambda = 80\,\mu$m period array of $h = 50\,\mu$m deep annular recesses with inner radius $a_{in} = 10\,\mu$m and outer radius $a_{out} = 30\,\mu$m. Vertical side walls are achieved by first forming a metal mask on the substrate a metal mask defining the desired pattern to the substrate prior to coating with resist. The resist is then exposed through the substrate mask, with which it is in perfect contact, with the aid of an UV I-line filter.

An annular blind hole in a metal sheet has some of the properties of a coaxial waveguide and, for sufficient depth (in this case $> 30\,\mu$m), supports a TEM-like mode bound to the central pillar and a TE_{11}-like mode localized at the edge of the hole. The TEM cut-off frequency is determined by the hole depth and is calculated to be just below 1.1 THz. The TE_{11} cavity cut off is mainly governed by the average groove diameter, $f_c \sim c/\pi a_{avg} = 2.4$ THz. This is above that of the zone boundary at $f_{ZB} = c/2\Lambda = 1.875$ THz and the calculated effective cut off lies just below f_{ZB}, at 1.79 THz. Propagating surface waves are associated with the evanescent fields below cut off so that the structure supports TEM and TE_{11} character surface modes, which are increasingly strongly confined as the frequency approaches cut off.

The surface waves were experimentally studied in the near field. Radiation was end-fire coupled into the guided modes of the 40 mm long, 6 mm wide structure using a cylindrical silicon lens and detected with a 10 μm dipole probe with integrated 20 μm aperture as shown in Fig. 9(c).

Fig. 10(a) shows an intensity map of time domain traces obtained at different heights z above the sample surface and a distance $x = 40\,\mu$m beyond the end of the sample. To a first

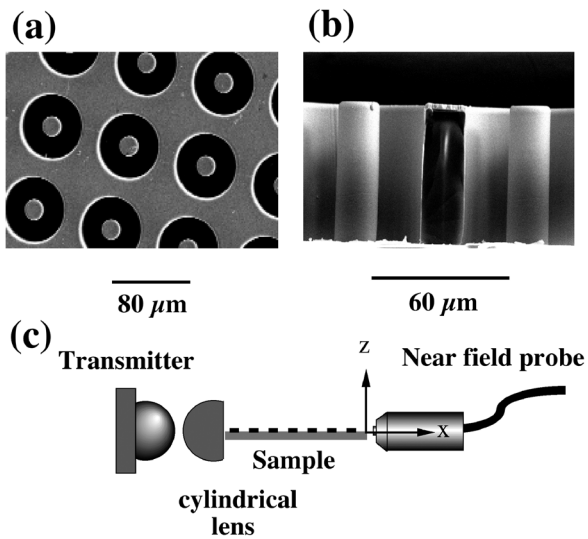

FIG. 9. (a) Electron micrograph of top surface of the metamaterial waveguide. (b) Cross section of the guide showing vertical side walls. (c) Schematic of end-fire coupling and near field probing arrangement and coordinate system

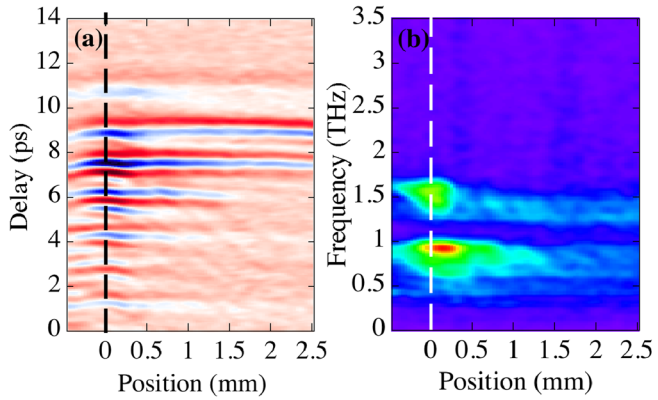

FIG. 10. (a) Map showing out of plane electric field versus delay at different z positions above the metamaterial surface plane and $x = 40\,\mu$m beyond the end of the guide. Red represents positive amplitude, blue negative and white zero. (b) Spectra versus z position. Blue is minimum and red is maximum amplitude. The plane of the sample surface is shown by the dashed lines.

approximation, this can be viewed as a map of the z component of the electric field at the point of launching into free space. The oscillations in the time traces are associated with dual band propagation in the TEM and TE_{11} character modes described above. This is shown more clearly in the corresponding spectral map shown in Fig. 10(b).

Fig. 11(a) shows a section through Fig. 10(b) at $z = 100\,\mu$m and x = 40 μm calculated using the finite integration technique with a 3 THz bandwidth input pulse. The calculated spectrum for the TEM mode is narrower and shifted to higher frequency compared with experiment, probably because of slight differences between the nominal and actual structures arising from non-uniform resist thickness. The calculated spectra are not very sensitive to the exact choice of x. The ratio of the integrated areas under the TEM and TE peaks is however similar in experiment and calculation. A further section through Fig. 10(b) is shown in Fig. 11(b). This displays the measured variation in the z component of the field for the TEM surface mode at the spectral peak of 0.9 THz. Also shown are calculations at a spread of frequencies around 0.965 THz, which is the spectral peak in the calculation. The calculations are of the field in air and ignore the structure of the probe. Taking into account the spectral

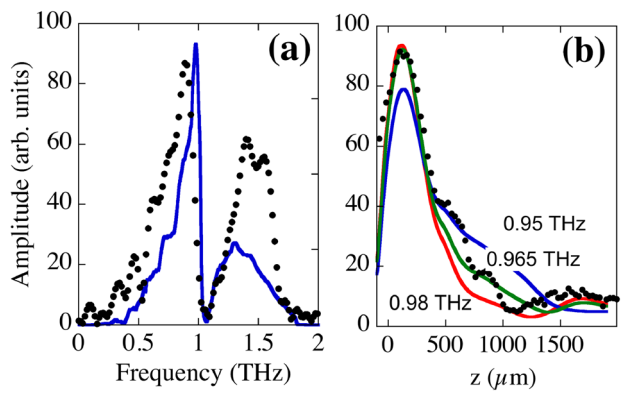

FIG. 11. (a) Comparison of calculated (solid curve) and measured (points) near field spectra for the metamaterial waveguide at a point $z = 100\,\mu$m above the surface and $x = 40\,\mu$m beyond the output end. (b) Measured and calculated peak to peak amplitude versus height above the surface at $x = 40\,\mu$m.

differences, the agreement between the field profiles in experiment and calculation is very reasonable. If the probe is included in the calculation then simulations show that the main perturbing effect is simply one of spatially uniform screening of the field. Thus, in this application, imaging artefacts are not significant.

B. Stepped parallel plate waveguide

We now briefly describe a simpler example of a parallel plate waveguide with a step discontinuity in plate separation, which illustrates how degenerate waveguide modes can be more easily distinguished in the near field than in the far field. The parallel plate waveguide has been extensively studied at THz frequencies because of its very low dispersion and relatively low loss.[46,47] Neglecting field penetration into the metal, the fundamental mode of a uniform parallel plate guide is TM_0 (TEM) with constant electric field perpendicular to the plates. The TM_1 mode is not excited with a symmetrical Gaussian input beam but can easily be observed in the step guide because of the broken symmetry. A hyper hemi-cylindrical silicon lens was used to couple a collimated THz beam into a 25 mm long parallel plate brass waveguide with flat, polished end faces in a similar end-fire geometry to that shown in Fig. 9(c). The input polarization was perpendicular to the plane of the plates. One plate is machined flat and the other has a 500 μm step. The separation was 1100 μm over the first 5 mm and 600 μm over the final 20 mm of propagation. The cut off frequency of the TM_1 mode in the latter section is 0.5 THz.

A probe consisting of a 10 μm dipole antenna with integrated 50 μm aperture was positioned 25 μm from the output face and stepped across the gap between the plates in 50 μm increments to obtain the spatio-temporal map shown in Fig. 12(a). The leading part of the traces show an approximately constant peak electric field across the air gap characteristic of the TEM mode, as shown in Fig. 12(b) at a time delay of 3.3 ps. The existence of a large and delayed signal outside the geometrical gap region attests to an additional TEM-like propagating wave in the 25 μm gap between the probe and the waveguide end faces similar to that discussed previously.

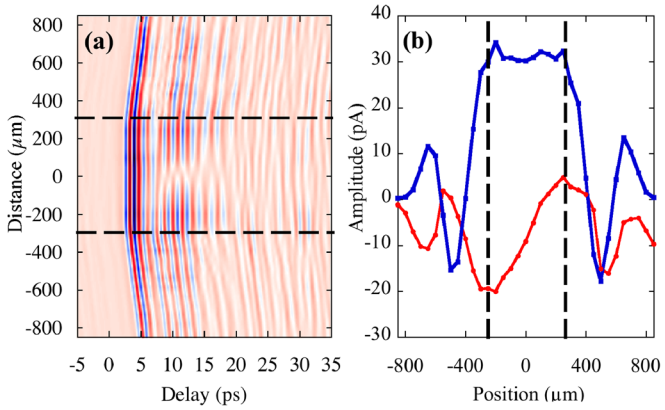

FIG. 12. (a) Spatial map at y = 0, showing time dependence of amplitudes versus probe position at the output end of the PPWG. The dashed lines show the limits of the waveguide air gap. Red colour indicates the positive field, blue negative and white zero. The two dashed lines indicate the air gap. (b) Sections through (a) at delays of 3.3 ps (blue curve) and 11.5 ps (red curve).

At later times in Fig. 12(a) there is clear evidence for the presence of more than one mode in the waveguide. At a delay of 11.5 ps, the field profile is anti-symmetric, suggesting that the TM_1 mode is also present.

VI. CONCLUSIONS

In summary, we have shown how the interaction between photoconducting dipole type THz near field probes and the system being studied is generally more complicated than simple screening but that electromagnetic simulations are a powerful aid to interpretation, given sufficient a priori knowledge of the system. Such simulations can be considerably simplified, without significant loss of accuracy, by treating metals as perfect electric conductors. We have also shown how the beneficial dispersion and power handling properties of hollow core photonic crystal fibre can be used to improve and simplify the construction of fibre coupled THz systems where freely positionable sources or detectors are required. Applications of the photoconductive probe are currently limited not only by the effects of sample probe interaction but also by the practical difficulties associated with the fragility of the probe and control of the sample-probe separation during imaging. These are often more of a limitation than the signal to noise ratio.

ACKNOWLEDGMENTS

We would like to thank H. Beere and D. A. Ritchie for kindly providing the low temperature GaAs used to make the probes and J. C. K. Knight for supplying the photonic crystal fibre. We also acknowledge useful correspondence with O. Mitrofanov and M. Walther. Financial support was provided by the Royal Society and the Airforce Office of Scientific Research.

[1]X.-C. Zhang and J. Xu, *Introduction to Terahertz Wave Photonics* (Springer, New York, 2010).
[2]B. B. Hu and M. C. Nuss, Opt. Lett. **20**, 1716 (1995).
[3]A. J. L. Adam, J. M. Brok, M. A. Seo, K. J. Ahn, D. S. Kim, J. H. Kang, Q. H. Park, M. Nagel, and P. C. M. Planken, Opt. Express **16**, 7407 (2008).
[4]A. Bitzer, H. Merbold, A. Thoman, T. Feurer, H. Helm, and M. Walther, Opt. Express **17**, 3826 (2009).
[5]O. Mitrofanov, T. Tan, P. R. Mark, B. Bowden, and J. A. Harrington, Appl. Phys. Lett. **94**, 171104 (2009).
[6]J. B. Pendry, L. Martin-Moreno, and F. J. Garcia-Vidal, Science **305**, 847 (2004).
[7]C. R. Williams, S. R. Andrews, S. A. Maier, A. I. Fernandez-Dominguez, L. Martin-Moreno, and F. J. Garcia-Vidal, Nature Photon. **2**, 175 (2008).
[8]O. Mitrofanov, I. Brener, R. Harel, J. D. Wynn, L. N. Pfeiffer, K. W. West, and J. Federici, Appl. Phys. Lett. **77**, 3496 (2000).
[9]S. Hunsche, M. Koch, I. Brener, and M. C. Nuss, Opt. Commun. **150**, 22 (1998).
[10]F. Keilmann, Infrared Phys. Technol. **36**, 217 (1995).
[11]Q. Chen, Z. Jiang, G. X. Xu, and X.-C. Zhang, Opt. Lett. **25**, 1122 (2000).
[12]A. Bitzer, A. Ortner, and M. Walther, Appl. Opt. **49**, E1 (2010).
[13]M. Wächter, M, Nagel, and H. Kurz, Appl. Phys. Lett. **95**, 41112 (2009).
[14]K. Wynne and D. A. Jaroszynsski, Opt. Lett. **24**, 25 (1999).
[15]Y. Cai, I. Brener, J. Lopata, J. Wynne, L. Pfeiffer, J. B. Stark, Q. Wu, X. C. Zhang, and J. Federici, Appl. Phys. Lett. **73**, 444, (1998).
[16]V. Astley, H. Zhan, R. Mendis, and D. M. Mittleman, J. Appl. Phys. **105**, 113117 (2009).
[17]N. C. J. van der Valk and P. C. M. Planken, Appl. Phys. Lett. **81**, 1558 (2002).

[18]H.-T. Chen, R. Kersting, and G. C. Cho, Appl. Phys. Lett. **83**, 3009 (2003).
[19]L. Guestin, A. J. L. Adam, J. R. Knab, M. Nagel, and P. C. M. Planken, Opt. Express **17**, 17412 (2009).
[20]M. Misra, S. R. Andrews, and S. A. Maier, Appl. Phys. Lett. **100**, 191109 (2012).
[21]NOA 61, *Norland Products* (Cranbury, NJ, USA).
[22]E. Yablonovitch, D. M. Hwang, T. J. Gmitter, L. T. Florez, and J. P. Harbison, Appl. Phys. Lett. **56**, 2419 (1990).
[23]J. C. Knight, Nature **424**, 847 (2003).
[24]P. Luan, J. C. Knight, P. St. J. Russell, S. Campbell, D. Xiao, D. T. Reid, B. J. Mangan, D. P. Williams, and P. J. Roberts Opt. Express **12**, 835 (2004).
[25]S. A. Crooker, Rev. Sci. Instrum. **73**, 3258 (2002).
[26]J. V. Rudd, D. Zimdars, and M. Warmuth, Proc. SPIE **3934**, 27 (2000).
[27]Y. Lee, S. Tanaka, N. Uetake, S. Fujisaki, R. Inoue, and M. Tonouchi, Appl. Phys. B **87**, 405 (2007).
[28]A. Dreyhaupt, S. Winnerl, T. Dekorys, and M. Helm, Appl. Phys. Lett. **86**, 121114 (2005).
[29]R. Thapa, K. Knabe, K. L. Corwin, and B. R. Washburn, Opt. Express **14**, 9576 (2006).
[30]P. G. Huggard, C. J. Shaw, J. A. Cluff, and S. R. Andrews, Appl. Phys. Lett. **72**, 2069 (1998).
[31]S. R. Andrews, A. Armitage, P. G. Huggard, and A. Hussain, Phys. Med. Biol. **47**, 3705 (2002).
[32]F. Formanek, M.-A. Brun, T. Umetsu, S. Omori, and A. Yasuda, Appl. Phys. Lett. **94**, 21113 (2009).
[33]See www.cst.com for CST Microwave Studio, Computer Simulation Technology, Wellesley Hills, MA, USA.
[34]M. A. Ordal, R. J. Bell, R. W. Alexander L. L. Long, and M. R. Querry, Appl. Opt. **24**, 4493 (1985).
[35]M. A. Leontovich, *Investigation of Propagation of Radio Waves, Part II*. (USSR Acad. Sci., Moscow, 1948).
[36]Y. Leviatan, J. Appl. Phys. **60**, 1577 (1986).
[37]C. J. Bouwkamp, Philips Res. Rep. **5**, 321 (1950).
[38]O. Mitrofanov, M. Lee, J. W. P. Hsu, L. N. Pfeiffer, K. W. West, J. D. Wynn, and J. F. Federici, Appl. Phys. Lett. **79**, 907 (2001).
[39]J. Federici, O. Mitrofano, M. Lee, J. W. P. Hsu, I. Brener, R. Harel, J. D. Wynne, L. N. Pfeiffer, and K. W. West, Phys. Med. Biol. **47**, 3727 (2002).
[40]F. Buergens, G. Acuna, C. H. Lang, S. Manus, and R. Kersting, Rev. Sci. Instrum. **78**, 113701 (2007).
[41]R. Mueckenstein and O. Mitrofanov, Opt. Express **19**, 3212 (2011).
[42]T.-I. Jeon, J. Zhang, and D. Grischkowsky, Appl. Phys. Lett. **86**, 161904 (2005).
[43]A. Bitzer and M. Walther, Appl. Phys. Lett. **92**, 231101 (2008).
[44]C. R. Williams, M. Misra, S. R. Andrews, S. A. Maier, S. Carretero-Palacios, S. G. Rodrigo, F. J. García-Vidal, and L. Martín-Moreno, Appl. Phys. Lett. **96**, 011101 (2010).
[45]See www.michrochem.com for SU-8 photoresist, MichroChem Corp., Newton, MA, USA.
[46]R. Mendis and D. Grishkowsky, Opt. Lett. **26**, 846 (2001).
[47]J. Liu, R. Mendis, and D. M. Mittleman, Appl. Phys. Lett. **98**, 231113 (2011).